Visualizing Strain Anisotropy in Mantle Flow Fields

H. Obermaier[1], M. I. Billen[1], H. Hagen[2], M. Hering-Bertram[3], and B. Hamann[1]

[1]University of California, Davis, USA
[2]University of Kaiserslautern, Germany
[3]Rhine-Waal University of Applied Sciences, Germany

Abstract
The evolution of strain and development of material anisotropy in models of Earth's mantle flow convey important information about how to interpret the geometric relationship between observation of seismic anisotropy and the actual mantle flow field. By combining feature extraction techniques such as path line integration and tensor accumulation, we compute time-varying strain vector fields that build the foundation for a number of feature extraction and visualization techniques. The proposed field segmentation, clustering, histograms, and multi-volume visualization techniques facilitate an intuitive understanding of three-dimensional strain in such flow fields, overcoming limitations of previous methods such as 2D line plots and slicing. We present applications of our approach to an artificial time varying flow data set and a real world example of stationary flow in a subduction zone and discuss the challenges of processing these geophysical data sets as well as the insights gained.

Categories and Subject Descriptors (according to ACM CCS): I.6.6 [Computer Graphics]: Simulation Output Analysis—

1. Introduction

Vector field visualization has received strong attention in the recent history of scientific visualization, as flow simulation techniques have become available to a diverse set of application areas. While the best known application fields for flow simulation such as aerodynamics and industrial mixing have been studied extensively from a visualization point of view, other fields such as geophysics suffer from a lack of specific visualization techniques and require the definition and development of alternative and tailor-made visualization methods.

Solid Earth geodynamics is concerned with the forces that move tectonic plates at the planet's surface through energy provided by solid-state thermo-chemical convection in the mantle (outer 2890 km). Over long periods of time ($> 10,000$ - 1 million years) and at the high temperatures and pressures of the mantle, material deforms by a process of solid-state creep flow at high effective viscosity (10^{19} - 10^{25} Pa-s). Due to the long time-scales and slow (< 10 - 100 cm/yr) non-inertial flow resulting from the high viscosity, the point of interest shifts away from classic flow field illustration, such as integral structure and vortex core extraction, towards visualization of more general continuum mechanics including object deformation, and the applicability of generic flow visualization techniques is rather limited.

In this paper, we are concerned with upper mantle flow (< 670 km depth) in subduction zones, where one tectonic plate sinks beneath another tectonic plate (e.g., Alaska, Japan). These subduction zones are of high importance to geoscientists because they provide the largest forces driving plate tectonics and are the most seismically active regions on the planet. One of the major outstanding questions regarding subduction zones is the geometry of mantle flow induced by sinking of a dense tectonic plate into the mantle [Bil08], which cannot be observed directly. Observations of seismic anisotropy provide indirect evidence of this pattern, because the crystal axis of the seismically anisotropic mineral olivine will align (i.e., they form a lattice preferred orientation (LPO)) with the strain direction during deformation. However, these observations must be interpreted with the aid of simulations of mantle flow, which track the evolution of strain and material alignment.

Our work aims at solving the problem of 3D flow-induced strain analysis by integrating a combination of feature extraction and field processing techniques with novel methods of strain segmentation and visualization. The resulting visu-

alization of flow and strain helps geoscientists in two ways. Firstly, it allows the scientist to distinguish regions with uniform strain orientations, which can be analyzed with a simple algorithm for comparison to observations, from more complex regions requiring more detailed analysis. Secondly, it facilitates rapid identification of the relative orientation of the strain orientations and the flow-field, which provides for more accurate interpretation of seismic anisotropy observations to determine the flow field. As a consequence, our work contributes both to the application field of geophysics by providing an intuitive and interactive visualization for flow induced strain analysis as well as to the visualization community by introducing novel methods for non-directed strain axis field segmentation and strain and cluster visualization.

The remainder of this paper is structured as follows: Section 2 gives an overview of existing visualization methods in the area of geophysics and strain visualization. In Section 3, background information on geological subduction and data formats are provided. Section 4 details the steps of strain field computation. Segmentation and visualization of the resulting strain fields are explained in detail in Sections 5 and 6. This is followed by an application and results section presenting the created results and their benefits for the geophysics community. Section 8 concludes this paper.

2. Related Work

Work related to the scope of this paper can be found in the field of visualization, where it is centered on visualization of vector and tensor fields and is partially related to strain analysis and in the field of geophysics, where basic techniques are used for visual analysis of flow and strain data.

Visualization Different flow visualization techniques are related to properties of flow induced strain. One such method is the *Finite Time Lyapunov Exponent* (FTLE) [Hal01] which derives a scalar valued convergence and divergence map from flow fields. The maximal structures of this field highlight regions where strain along a particle trajectory is locally maximal, thus giving an insight into flow separation. Contrary to FTLE, which is based on gridded integral line generation, others [OHBKH09] have proposed visualizing strain that was accumulated along individual integral flow lines to visualize deformation of distinct volume particles over time. This technique has recently been applied to generate a localized FTLE map [KPH*09]. The work presented in this paper makes use of a similarly dense and localized line integration to obtain strain directions in time-varying flow fields. In tensor field visualization and *Diffusion Tensor Imaging* in particular, anisotropy clustering based on tensor invariants with varying distance measures is state-of-the-art and has been proposed by several authors [ZMB*03, STS07, RJF*09]. Their clustering methods are fine tuned for DT-MRI tensor fields. In the context of geophysics, stress-related tensors have been visualized

by glyphs in [NJP05]. In the last years, strain segmentation has received increased attention in vector field visualization by the definition of various Eulerian and Lagrangian strain measures, which have been used to segment flow fields into strain and vortex regions based on the magnitude of these components [SWTH07]. For a state-of-the-art report on volume visualization we refer to [EHK*04].

Geophysics Analysis of *Lattice Preferred Orientation* or grain orientation [ZiK95] obtained from mantle flow simulations of subduction zones [JB10, WSMG06] is commonly performed by manual inspection of generic visualizations resulting from techniques such as slicing and arrow plot visualization [JB10] of instantaneous *Infinite Strain Axis* directions [JB10, KR02]. While these visualization methods are generally available and easy to implement, they suffer from loss of dimension and lack a homogeneous field impression. The need of manual parameter adjustment such as slicing orientation and position favors overlooking of features during visual inspection. A first attempt at computing and interpreting LPO from time-varying flow simulations was done in [MvKK02] by the integration of strain along particle tracers. The resulting two-dimensional strain orientation field is visualized using line plots and temperature based coloring and serves as basis for further manual analysis and segmentation. Work with focus on visualization of geophysical flow with analysis of heat and critical point development is given by [EYD02]. A natural two-dimensional watershed-like visualization of LPO is given by optical micrographs with polarized light [ZiK95] and is the result of photographing physically sliced material samples in lab experiments. FTLE-like visualizations are presented in [Sub09].

3. Strain in Geophysical Flow Data

In simple flow fields, such as horizontally oriented simple shear found beneath the center of large tectonic plates, it is appropriate to assume that the orientation of LPO, or observed seismic anisotropy, and the flow field is parallel [CBS07]. However, in subduction zones, the flow-field can be highly three-dimensional depending on the geometry of the subducting plate [JB10] and can change rapidly in time [BB10]. An observation of seismic anisotropy provides a single measurement at the Earth's surface that reflects the changing pattern of seismic anisotropy along the ray path of the seismic wave in the upper mantle, as illustrated in Figure 1. Therefore, accurate interpretation of this observation requires knowing how the pattern of material alignment varies spatially and how it relates to the geometry of the flow field.

3.1. Background

Simulation of subducting slab movement and evolution of LPOs enables geophysicists to make predictions about the propagation of seismic waves caused by earthquakes or artificial sources. Observation of differences in the speed of
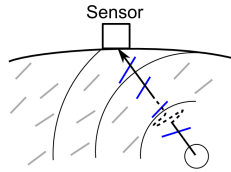
Figure 1: A seismic wave travels through the Earth's mantle before reaching a sensor at the surface. LPO along the ray (in blue) are used as approximation of mantle flow geometry.

propagation of polarized seismic waves is one method of inferring the pattern of mantle flow [RS94]. Such seismic anisotropy occurs in the upper mantle in regions where deformation causes the crystal lattice within olivine minerals to acquire a preferred orientation. Bulk alignment of this mineral's crystal structure will cause seismic waves that travel through these regions to arrive at seismic stations at different times depending on wave polarization. From this information seismologists can geographically map bulk alignment in the mantle, which is usually indicated by plotting the direction of the fastest seismic axis of the olivine mineral, providing a first rough approximation of mantle flow directions.

The relationship between the mantle flow pattern, the shearing causing the alignment, and the resulting fast-axis depends on several other factors [KJKS08]. When neglecting microscopic influence on material orientation such as recrystallization, these directions of preferred alignment may be approximated by deformations caused by macroscopic external forces such as strain induced by the flow field [WSMG06]. In addition, the magnitude of stretching is also important because significant shearing is needed to cause the lattice orientation to become both strongly aligned and pervasive throughout the bulk rock: only pervasive and strong alignments can be seismically detectable. Limitations on joint analysis of the numerical models and the seismological data stem mainly from the difficulty in clearly identifying the 3D geometries of regions where strong lattice preferred orientation is predicted by the numerical models and providing this information to seismologists so they can more accurately interpret the observations. This is due to the fact that previous studies linking seismic lattice preferred orientation with mantle flow have been limited in their ability to compare the complex 3D patterns of stretching found in numerical models with the surface observations of seismic fast axis directions. Most studies have made simplifications such as focusing on two-dimensional map slices or cross sections of the stretching directions (see Figure 2), ignoring the effects of dipping fast axis, or interpreting only the large-scale patterns [CBS07, JB10, MvKK02].

During data set analysis, geophysicists have to identify regions with different strain orientation as well as regions with high anisotropy manually to make estimations about predicted seismic wave propagation. The inevitable requirement of manual plane alignment as well as visual ambiguities and clutter resulting from common visualization methods based

on slicing complicates data set analysis. We aim to develop methods to assist and support geophysicists in their analysis of seismic anisotropy. In summary, the methods introduced in this paper have the following two goals:

- Visualize time-varying and stationary strain orientation (i.e., material alignment) discontinuities to separate heterogeneous regions and allow identification of persistent strain forces.
- Visualize correlation between flow direction and material alignment in the simulated flow field to allow verification and analysis of mantle flow directions as obtained by real-world seismic measurements.

Consequently, the proposed visualization methods presented in the next sections not only rely on the data provided by the velocity vector field but make use of the accompanying stress tensors as well.
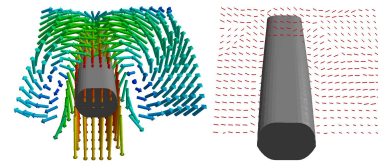

Figure 2: Typical slicing techniques showing flow direction and magnitude (left) and predicted LPO orientation (right).

3.2. Data Format

Mantle flow simulation data in this work is given on an irregularly spaced curvilinear grid in a geographic coordinate system and represents mantle flow in a small section of Earth as seen in Figure 3a. For computational reasons, we map this geometric data in a pre-processing step from locally rotated geographic coordinate systems to a global Cartesian coordinate system by applying $X : (\psi, \phi, r) \rightarrow (x, y, z)$. The neighborhood relation between data points is not affected by this mapping. Cells of the data set are identified by indices (i, j, k) with irregular spacings in longitude, latitude and radius direction. To guarantee correct cell identification and avoid errors that would occur when evaluating the field in the now distorted neighborhood grid, positions during field evaluation in $\mathbb{R}^3$ are mapped back into the curvilinear grid by X^{-1}. The correct surrounding cell of the evaluation point is subsequently identified by binary search in the grid intervals of longitude, latitude and radius (see Figure 3b). Cell based interpolation is performed in local geographic space.

4. Strain Field Computation

The main goal of this paper is the analysis of material alignment, as induced by the flow field. For this matter, this section introduces a method that facilitates the computation of such strain orientations at arbitrary positions in space and time by integration of the velocity gradient. The resulting field of material alignment directions is termed a *strain field* and is used to extract alignment discontinuities and evaluate
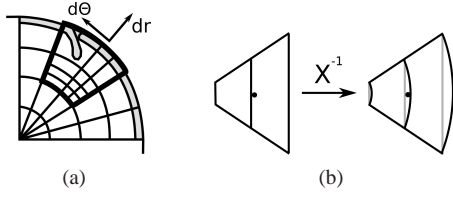
Figure 3: (a) Two-dimensional illustration of possible data set locations in geographic coordinates. One section of the data set contains a subduction zone in the upper mantle.
(b) Points of evaluation are mapped back into the original curvilinear field before cell-wise interpolation is performed. This avoids incorrect cell identification and allows interpolation in geographic coordinate space.

mantle flow directions. Thus, the general notion of a strain field as used in this work is that of a vector field whose orientation corresponds to the direction of main deformation of Lagrangian particles. In the following we assume that all regions where significant deformation takes place are contained in the simulation domain. To compute this deformation, we release isotropic particles into the flow field at regions of inflow and deform them along their paths according to strain in the flow field. The strain direction of a particle is then computed from the resulting anisotropic shape. Given a sufficiently dense particle set, strain directions at arbitrary positions in time and space can be reconstructed by interpolation. These strain axes approximate preferred material alignment in geophysics caused by macroscopic external forces. In the following we detail the steps of strain field computation.

4.1. Strain Tensors

Simulations of the geodynamic model commonly return flow, temperature, viscosity and symmetric stress data. The stress-strain relationship of non-Newtonian fluids is non-linear, and strain at different stress levels exhibits varying behavior such as viscous or plastic deformation [JB10]. If the model of stress-strain relationship is known, the strain rate tensor field can be accurately obtained from the input stress field and given viscosity. In a more general case, the infinitesimal strain rate tensor may be computed by decomposing the velocity gradient of the flow field into a rotational antisymmetric and a symmetric part. For a 3D vector field $v : \mathbb{R}^3 \to \mathbb{R}^3$, the velocity gradient may be approximated by finite differences (1) and decomposed into the rate of strain S and rate of rotation R tensors (2). This rate of strain tensor S is a linear approximation of deformation caused by Eulerian or Lagrangian strain:

$$(\nabla v)_{ij} = \frac{v_j(x+h \cdot e_i) - v_j(x-h \cdot e_i)}{2h} \qquad (1)$$

$$S = \frac{1}{2}(\nabla v + (\nabla v)^T) \qquad R = \frac{1}{2}(\nabla v - (\nabla v)^T) \quad (2)$$

Once the data set is mapped to Cartesian coordinates, we perform strain analysis with a desired level of detail according to the steps described in the next paragraph.

A uniform 3D Cartesian grid with a user specified voxel resolution is imposed on every time step of the data set. In time-varying data sets path lines are integrated such that every voxel in 4D is traversed at least once. This guarantees a minimum density of particles at every location in the data set. Particles traveling along these integral lines are subject to strain forces and thus change from a spherical to a deformed shape. The main axes of these strain ellipsoids define the direction of material alignment and are computed at every four-dimensional voxel of the field discretization. We segment the resulting strain axes field using different techniques to highlight distinct strain regions. Details on these segmentation steps are given in later sections.

4.2. Discretization of the Flow Field

As our time-varying strain mapping method requires that every cell of the final strain field grid is traversed by at least one path line, we let the user choose a resolution for this discretization to reduce computational complexity and support interactivity. Thus, we assume in the succeeding sections that the data set is superimposed by a Cartesian grid of $l \times m \times n$ voxels v_i per time step t. Resolution of the final strain orientation field is bound to the resolution of this discretization step, i.e., strain orientations are given per voxel.

4.3. Dense Path Line Integration

Strain orientation at a given point p in space and time is computed by accumulating strain information along a particle path that ends in p. As our method produces strain orientations per voxel similar to other image based visualization techniques like FTLE, it has to be guaranteed that every four-dimensional voxel v_i^t is traversed by at least one such particle path. To satisfy this requirement, one particle path, i.e., one path line, is started at the centroid of every voxel v_i^0 and integrated with an adaptive 4th-order Runge-Kutta integrator [TGE97] until it leaves the data set or reaches the last time step. During traversal voxels v_i^t are marked with the line and position index of the path line if a four-dimensional floating point rasterization [Bre65] of the path line crosses the voxel.

New path lines p_x are started at the center x of all unmarked v_i^t and integrated in forward and backward direction according to their standard definition (3).

$$p_x(t) = x + \int_0^t \pm v(p_x(\tau), \tau) d\tau \qquad (3)$$

After this stage of the algorithm, every voxel is traversed by at least one path line. Furthermore, every voxel knows the indices of traversing path lines and the closest preceding discrete position on the line as illustrated in Figure 4a.
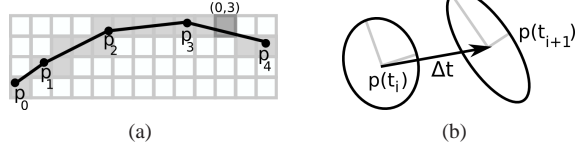

(a)   (b)

Figure 4: (a) Illustration of line rasterization. The highlighted cell knows line (0) and position index (3).
(b) Deformation of particle neighborhoods caused during particle advection. Major and minor eigenvectors of the deformed particles are shown in gray.

4.4. Orientation Field Computation

Let $p_x^t : \mathbb{R} \rightarrow \mathbb{R}^3$ denote the path line with starting position $p_x^t(t) = x$. Under the assumptions that a path line $p_{x_0}^{t_0}$ crosses a given position x^t at time t and that initial particle shapes are isotropic, strain orientation at x^t is defined as the direction of the major axis of the deformed particle at $p_{x_0}^{t_0}(t) = x^t$. The deformation tensor D defining the mapping from an initially spherical particle neighborhood to a deformed shape at $p_{x_0}^{t_0}(t)$ is computed by accumulation of strain information along discrete positions t_j of the integral particle trace $p_{x_0}^{t_0}$:

$$D_{x_0}^{t_0}(t) = \left(\prod_{j=0}^{i} exp(S(p_{x_0}^{t_0}(t_j)) \cdot (t_{j+1} - t_j)) \right) \cdot D_{x_0}^{t_0}(t_0) \quad (4)$$

with $t = t_i$ and an initially isotropic shape $D_{x_0}^{t_0}(t_0) = I$. The strain rate matrix given by the simulation at $p_{x_0}^{t_0}(t_j)$ is $S(p_{x_0}^{t_0}(t_j))$. The change in shape over an interval $[t_j, t_{j+1}]$ along the path line $p_{x_0}^{t_0}$ is captured by the matrix exponential $exp(S(p_{x_0}^{t_0}(t_j)) \cdot (t_{j+1} - t_j))$, as defined for a general matrix A by

$$exp(A \cdot \Delta t) = \sum_{i=0}^{\infty} \frac{1}{i!} A^i \cdot \Delta t^i. \quad (5)$$

The mathematical relationship described by Equation (4) is depicted in Figure 4b and has been used in stationary or first order form in [KR02, OHBKH09].

Length and direction of the major axis of the deformed ellipsoids at x^t are given by the square root of the maximum eigenvalue and the corresponding eigenvector of $D_{x_0}^{t_0}(t)^T \cdot D_{x_0}^{t_0}(t)$.

Based on these definitions and the information collected during particle tracing, it is feasible to compute the desired strain axis orientation field for arbitrary time steps. Values of the strain field are computed at the center of every voxel v_i^t by evaluating (4) at the closest point on a path line that crosses this voxel and interpolating it in a nearest neighbor fashion. We note that a four-dimensional position x has a unique path-line passing through it if the field is Lipschitz continuous. If no path-line passes through the center and the closest path-line is not unique, we average strain directions of all closest path-lines. The direction of the major axis represents our strain axis orientation at v_i^t, magnitude of the field corresponds to the largest eigenvalue of $D^T \cdot D$.

4.5. Stationary Strain Fields

Unlike the Lagrangian strain analysis presented in the preceding sections, geophysicists often simplify LPO computation by analyzing instantaneous strain distributions. Further reasons to work with stationary flow fields are the large time-scales as well as missing availability of time-varying data sets. The concept of *infinite strain axis* analysis [KR02] facilitates local strain axis computation that successfully approximates a complicated Lagrangian strain advection in many real world situations. Thus, the instantaneous strain orientation field is calculated as a local approximation of the asymptotic major axis of the strain ellipsoid after an infinite amount of constant strain. The methods described later in this paper are suitable for analysis of strain orientation fields resulting from time-varying and stationary fields.

5. Strain Field Segmentation

The visualization goals specified in Section 3.1 require the highlighting of strain discontinuities and velocity-strain relationships. We satisfy these requirements by segmenting the field into regions with homogeneous strain orientation or homogeneous strain-velocity relationship. The following sections present two criteria for strain segmentation to achieve this goal and aid analysis of important LPO properties.

As the main direction of strain corresponds to expected lattice preferred orientation, strain segmentation in the context of this work focuses on this direction only [ZTW06], rather than on other tensor properties [LGALW09]. The set of strain orientations in a given time step defines a non-directed vector field $g : \mathbb{R}^3 \rightarrow \mathbb{R}^3$. Positions, where the deformed particles are isotropic and no unique strain orientation exists, are treated as a separate group, i.e., they exhibit maximal dissimilarity to other strain orientations.

5.1. Orientation Segmentation

To allow analysis of regions of LPO discontinuities, we capture rapid changes in LPO by computing the Frobenius norm of the Jacobian of the normalized gradient field $g^* = \frac{g}{\|g\|}$:

$$f_o(p) = \sqrt{\sum_{i=0}^{3} \sum_{j=0}^{3} \left(\frac{\partial g_i^*(p)}{\partial x_j} \right)^2} \quad (6)$$

Due to the normalization of g, $f_o(x,y,z)$ represents a measure of angular deviation of the strain axis field g in a neighborhood of p. Thus, maxima of f_o describe regions with a sudden change in strain orientation. We approximate the Jacobian by difference quotients with locally oriented strain axis directions.

The voxel grid together with values of f_o creates a 3D scalar valued image that can be used as basis for domain segmentation. We use interactive watershed segmentation to extract locally maximal structures [RM00]. All results shown in this paper use a watershed-segmentation level that merges small scale basins with depth < 10% of the data range.

5.2. Alignment Segmentation

A second important property of strain fields is the degree of alignment between strain and velocity direction. This is especially important in areas, where one of the two fields is used to derive information about the other, as is the case in seismic analysis of LPOs. Such seismic analysis is concerned with identifying lattice preferred orientations and deducing appropriate mantle movement. For this matter, we map g to a scalar field representing the angular difference between strain and velocity:

$$f_a(x,y,z) = acos\left(\frac{|g(x,y,z)^T v(x,y,z)|}{||g(x,y,z)||||v(x,y,z)||}\right) \quad (7)$$

Segmentation of the range of f_a induces a segmentation on the strain field itself. A segmentation of the strain field with respect to f_a is performed by applying thresholding to the range of f_a, thus subdividing the alignment interval $[0, \pi/2]$ into smaller segments. In contrast to FTLE visualization, where segmentation or highlighting of strain magnitude is desired, f_a can be used to separate flow parallel deformation from flow orthogonal regions of deformation. High values of f_a indicate a strong divergence between strain and flow direction and can provide guidance as to the level of analysis required to accurately interpret observed seismic anisotropy in corresponding regions of the data set.

6. Visualization

The goal of the visualization techniques presented in the following is to provide domain experts with the means to perform three-dimensional analysis of strain directions and overall field behavior without relying on two-dimensional projective methods such as slicing. For this matter, boundaries and shape of strain volumes resulting from the segmentation criteria defined in the previous sections as well as strain and flow behavior in the interior of these volumes have to be visualized while avoiding common problems of 3D visualization such as information overload, visual occlusion and clutter. Our visualization has to cope with these challenges while clearly depicting key features of the strain field.

A visualization technique for strain analysis in mantle flow fields should be able to convey the following key properties:

- Display boundary and shape of strain volumes
- Illustrate strain orientation and magnitude in the interior of strain volumes
- Show relative flow behavior
- Show local and global strain behavior

With this visual information, we enable domain experts to distinguish regions in which seismic anisotropy measurements are indicators of mantle flow directions from regions in which more detailed analysis is required to relate observations to flow geometry. In contrast to common strain visualization techniques that focus on glyph or hyperstreamline techniques [HJYW03] to visualize full tensor information, the techniques presented in this work combine visualization of major strain axis direction and field segmentation and make frequent use of transparency to reduce occlusion. To provide a spatial and global view of the strain and flow field, we combine statistical orientation visualization in the form of histograms with 3D display of strain directions and segmentation volumes. As transparency plays a major role in the display of strain volume shape and boundary, we use multi-volume rendering techniques to easily use correct order-dependent transparency on a volume and content level.

6.1. Multi-Volume Visualization

The distinct regions in image space as obtained by the methods described in Section 5, are sets of voxels and as such represent geometric volumes that segment the present data set into separate sections. To visualize both strain orientations and boundary shapes of segmentation geometry, transparent rendering of these volumes is required. Correct rendering of segmentation geometry in the form of transparent boundary surfaces may be performed by methods such as depth-peeling [Eve01] or order dependent rendering. However, when combining this visualization with a volume rendering of internal strain orientation, one quickly runs into problems with respect to correct transparency rendering [RTF*06]. As a consequence, we use a multi-volume visualization technique comparable to [HBH03] for consistent and interactive rendering of both internal strain and segmentation geometry based on volume slicing and clipping [WEE02].

A segment or subvolume V_i defines a binary mapping on the data set, classifying individual voxel centers as interior or exterior. We store values of this binary map $m_i : \mathbb{R}^3 \to \{0,1\}$ as 3D mask in the form of alpha values of a RGBA texture, where entries of the RGB vector in the vicinity of volume boundaries represent geometric normals of the volume geometry, as seen in Figure 5. Trilinear interpolation on m_i yields a representative volume definition for the isovalue 0.5.

Utilizing this data and the well-known Marching Cubes (MC) algorithm, we perform the following steps for slicing-

based [EHK*04] selective multi-volume visualization (see Figure 5):

1. Create individual volume mask textures from m_i.
2. Determine extremal depths z_{max} and z_{min} for bounding box of volume set for current view and volume positions.
3. Subdivide $[z_{min}, z_{max}]$ into $n+1$ intervals with length Δd.
4. Compute MC slice geometry t_{iso} for every volume and current isovalue $iso = z_{max} - \Delta d$.
5. For every t_{iso}: render transparent slice by passing mask, position and representation of flow and strain directions of sliced volume to fragment shader.
6. Repeat from 4. with $z_{max} = z_{max} - \Delta d$.

Slice geometry for a volume V_i obtained in step 4 is processed in a fragment shader with corresponding mask and position data, where all geometry and volume information outside of the volume ($m_i(x, y, z) < 0.5$) is discarded [EHK*04] and locations close to the boundary ($m_i(x, y, z) \in [0.5, 0.6]$) is rendered as volume boundary representation. Embedding the volume representations (e.g: bounding boxes) into a global depth-context allows consistent propagation of scalar values in step 2. Isovalue stepping together with "z-less or equal" depth buffer testing guarantees view-dependent and consistent back to front rendering of volumes with correct transparency processing.

This technique allows arbitrary selection and positioning of individual parts of the volumetric data set, has the advantage of preventing classic z-fighting issues when using pre-sorted triangulated geometry, and avoids expensive plane-clipping, sorting or intersection computations, allowing highly interactive framerates.
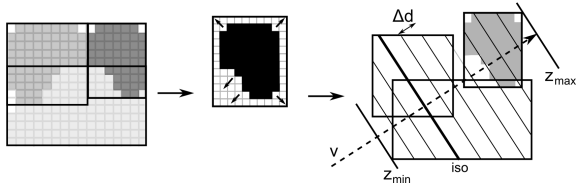

Figure 5: Steps of MC-based multi-volume slicing and visualization. First, a RGBA mask with normal information is created for each subvolume. In the final volume composition, view dependent scalar- and isovalue propagation is performed for MC slicing and allows fast and correct multi-volume visualization for arbitrary volume positions in $\mathbb{R}^3$.

6.1.1. Volume Boundaries

Volume boundaries are defined as regions close to the boundary of the volume mask ($m_i(x, y, z) \in [0.5, 0.6]$) and are shaded with pre-computed normals stored in m_i. Each volume is assigned a color from HSV-color space.

6.1.2. Volume Interior: Strain Lines

Information on the inside of a strain volume consists of strain and velocity vectors. The complete strain field g for one instance in time corresponds to a typical eigenvector field as obtained from tensor data such as DT-MRI and represents a general non-oriented vector field. This field type allows extraction of integral lines along strain directions. To visualize strain directions for a given time step of the simulation, we integrate a uniformly spaced set of lines L_i that are locally tangential to the direction of strain and rasterize them into a 3D texture. Use of a texture allows slicing-based volume visualization as described in the previous section. Opacity and color at a position $p = (x, y, z)$ defined by

$$Rgba(p) = \begin{pmatrix} 2 \cdot f_a(p)/\pi \\ 0 \\ 1 - 2 \cdot f_a(p)/\pi \\ ||g(p)|| \cdot max_i(\omega(d(p, L_i))) \end{pmatrix} \tag{8}$$

where d returns the distance between a point and a given line and $\omega(d) = e^{-\frac{d^2}{r^2}}$ is a spherical kernel function with constant radius r. A volume rendering of the resulting 3D strain texture produces pictures comparable to volume LIC [CL93], where strain magnitude/FTLE values are mapped to opacity and color to the degree of alignment between flow and strain direction (red: strong alignment, blue: orthogonality). Spacing of integral lines reduces typical occlusion problems present in volume LIC visualization. A texture containing these strain-lines is passed to the fragment shader in step 4, thus clipping strain lines outside of active volumes.

6.1.3. Interaction

As the proposed multi-volume visualization method allows selective display and transformation of parts of the data set, we implement hiding or deactivation of single volumes. To realize such color based picking in OpenGL, we extract geometric triangulations of volume masks (see Figure 5). This geometry is used for fast picking operations only and is not used for final visualization of the data set, due to limited suitability for transparency rendering.

To provide a clearer look at volume boundaries, we give the user control over volume positioning by making use of the explosion metaphor, allowing volume positions to change according to a force driven concept. Let $c_i^0 = c_i$ be the bounding-box center of strain volume $i \in \{1, \ldots, n\}$. Iterative evolution of volume centers is governed by:

$$c_i^{k+1} - c_i^k = h \frac{1}{\sum_j^n \omega(j, i)} \sum_j^n \omega(j, i) \frac{(c_i^k - c_j^k)}{||c_i^k - c_j^k||}$$

where $h > 0$ controls explosion step size and ω is a smooth distance based weighting function. Visual distinction between different strain volumes is aided by color coding. For non-strongly interleaved volume sets this positioning concept provides better views at volume and boundary shapes and simplifies selection of individual volumes. Additionally,

transparency of volume boundaries is a free, user controlled parameter and does not only give a clearer look at otherwise hidden volume boundaries due to the reduction of occlusion, but enables the user to have a look at interior properties of the volume by revealing strain lines.

6.2. Strain Histograms

While the presented multi-volume visualization technique gives a localized view of strain orientations, a more global view of these orientations and their segmentation is desired in strain analysis to identify prevalent and separated strain orientations. An established display method for global segmentation analysis in the field of image processing are histograms. Fortunately, histogram binning is not limited to scalar fields, but may be generalized and adapted to higher dimensional data types such as vector fields by the use of spherical histograms [GJL*09]. We use a similar technique for spherical histogram construction in our non-directed strain axis field.

6.2.1. Sphere Subdivision

Previous histogram methods use a uniform parameterization in spherical coordinate space to obtain bin intervals, leading to a high variation in bin sizes. Bin areas around the pole are degenerate and minimal, whereas areas along the equator are comparatively large and quadrilateral. This variation opposes the desire to use histograms as a consistent density measurement and visually cannot be fully compensated by scaling of bin heights. As a result of these observations, we prefer an almost equidistant parametrization of the sphere as given by icosahedron subdivision (see e.g. [HS05]). The resulting sphere subdivision resembles a geodesic dome consisting of almost equilateral triangles, thus allowing uniform data binning with almost identical base area. Further advantages of this parametrization are consistent triangular bin shapes in contrast to mixed rectangular and triangular shapes. A disadvantage of this subdivision is however the increased complexity of identifying corresponding bins for given normalized vector directions, since bin triangles do no longer correspond to regular subdivisions of longitude and latitude. To reduce this computational complexity, triangles of the icosahedron are assigned to cells in a uniform discretization of 3D space to allow fast-access bin hashing during histogram creation.

6.2.2. Data Binning

The orientation information of the strain axis field is reflected in the spherical histogram by mapping the height of right prisms to the number of orientation vectors pointing to its base triangle. This construction leads to a point-symmetric histogram in the case of non-directed vector fields; i.e., two mirrored hemispheres. Volume membership information gathered during strain field segmentation is mapped to the histogram by the use of volume colors. For this matter, each volume is assigned a distinct color from HSV space with $S = 1$ and $V >= 0.5$. During data binning, RGB bin color for a bin b is computed as scaled average of the contributing strain volumes:

$$(R,G,B)_b = \frac{\sum_i \chi_b(i)(R_{s(i)}, G_{s(i)}, B_{s(i)})}{\|\sum_i \chi_b(i)(R_{s(i)}, G_{s(i)}, B_{s(i)})\|} \qquad (9)$$

where χ_b is a binary membership function indicating whether a direction contributes to bin b and $s(.)$ returns the index of the volume a vector is associated with. Additionally, saturation of the resulting color is set to a value inversely proportional to the number of contributing volumes to avoid ambiguities. A histogram with a number of small distinctly colored and highly saturated regions with homogeneous color indicates that strain variation within single volumes is small.

6.2.3. Interaction

The spherical histogram associated with the data set responds to user selections in volume visualization mode. Contribution of orientation vectors located in inactive volumes are removed from the histogram bins. Fast histogram updates are guaranteed by storing volume contributions for every individual bin and volume during initial histogram construction. Removal of certain volume contribution in bin height and color can thus be performed quickly without triggering a full recomputation of the histogram. Reduced histograms enable the user to quickly observe strain orientations in a more local and focused context. Again, color-based picking is implemented to allow selection of individual bins. Selection of a set of bins b_i initiates the construction of a volume Ω in 3D space with $g^* : \Omega \to b_i$. This interaction allows interactive creation and highlighting of strain volumes. In contrast to the segmentation methods described in this paper, interactive selection can produce overlapping strain volumes. For interactive creation of f_a volumes, we implement a radial alignment display that allows selection of alignment intervals in $[0, \pi]$.

7. Results and Evaluation

This section discusses visualization capabilities of the presented methods as well as visualization benefits as identified by domain experts. Due to the difference in strain computation, we present results of stationary flow fields separately from time-varying strain analysis.

7.1. Visualization of Time-Varying Flow

For the analysis of time-varying strain behavior, we applied our method to a small region of a test model used to study the dynamic process of the detachment or break off of part of a sinking tectonic plate from the plate at the surface, as seen in

Figure 6 [BB10]. In this test case, the sinking tectonic plate is comparatively young with an age of around 20-30 million years, which means that it is fairly thin and weak compared to older tectonic plates. Therefore the sinking plate rapidly sinks vertically. Subducting slab geometry is approximated by a temperature isosurface. The flow of the mantle around the slab is dominated by two components: poloidal flow and toroidal flow, as seen in Figure 6. Each time-step of the simulation covers approximately 310,000 years. Figure 6 shows a volume visualization of rasterized strain lines by reducing opacity of volume boundaries to 0. Our visualization conveys convergence and divergence flow properties, as regions with dominant opacity correspond to Lagrangian Coherent Structures in FTLE fields. In contrast to standard FTLE methods, our technique includes directional information. In regions with strong alignment between flow and strain (red) strain and stream lines coincide, whereas flow is orthogonal to strain in blue regions. Figure 7 is a visualization of the evolution of selected f_o subvolumes of this data set. Homogeneous and consistent strain orientations can be seen on lateral parts of the slab path both in the volume display as well as in the histograms. Discontinuities in strain orientation develop mainly along paths of vortex cores. Localized histogram information gives an insight into expected seismic anisotropy for different regions. Results obtained by alignment segmentation are given in Figure 8. Strong disagreement in flow and strain alignment as extracted in Figure 8 is observable along outer regions of vortices and underneath the slab. Radial displays show distribution of alignments in the data set (y axis corresponding to full alignment) by color and opacity and current volume selection (blue segment).

7.2. Instantaneous Flow

The given instantaneous flow field covers a portion of a model of the southern Alaska subduction zone where the Pacific plate subducts beneath Alaska [JB10]. This model has predominantly vertically-oriented flow that is drawn in perpendicular to the top of the slab (poloidal flow) and horizontally-oriented flow around the edges of the slab (toroidal flow). The data set consists of around 5.7 million points carrying velocity, temperature, viscosity and stress information. Furthermore, a pre-computed set of infinite strain axis direction, as described in Section 4.5, is provided. Data dimensions are $[23°, 29°]$ for co-latitude $[205°, 220°]$ for longitude and $[5971\ km, 6321\ km]$ for radius. Results of our segmentation method on a 100^3 voxel grid is shown in Figure 9, where the benefits of interactive picking and volume explosion are demonstrated. Further visual improvement is gained by transparent rendering of volume boundaries, providing a look at inner strain directions. Volume visualization of the segmented data set with fully opaque boundaries visually corresponds to a triangulation based visualization. More details and clean segmentation of strain volumes can be obtained in high voxel grid resolutions. As listed in Table 1, a low resolution grid greatly reduces computation times,

Data set	50^3	60^3	100^3
Alaska	-/-/1.6	-/-/2.6	-/-/15.6
Simulation	2.0/3.2/1.3	3.3/5.3/2.0	10.0/16.4/4.6

Table 1: Average seconds (Intel Core2 Duo 2.16Ghz, 4GB RAM, 64bit) spent per time step on integration/tensor accumulation/segmentation for different resolutions of the grid.

caused by a decreased number of integrated path-lines and decreased number of velocity gradients. Segmentation time increases less rapidly with a higher resolution. We note that f_o segmentation of the field for identical watershed segmentation parameters converges, as the grid resolution is increased.
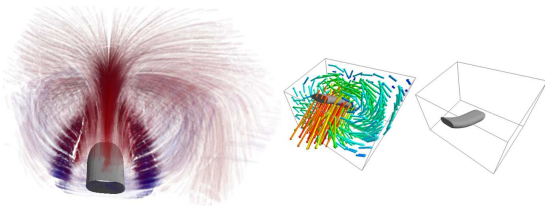

Figure 6: Left: Volume visualization of strain lines with fully transparent volume boundaries. Right: Sinking slab in test data set. Velocity magnitude is highest along the path of the slab, while slow rotating flow is observed along its sides.
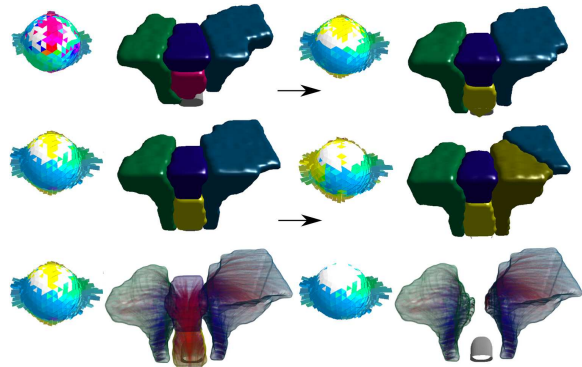

Figure 7: Left to right, top to bottom: Four time steps of evolution of prominent f_o features and histograms. Histogram information shows that strain in the two lateral regions is orthogonal and converges over time as the slab leaves the data set. Region splitting indicates forming of new regions with high strain discontinuity. Volume rendering conveys the impression of phong shaded solid geometry as well as transparent volumes with interior strain lines. Bottom row: Explosion and volume selection allow an unobstructed view at volume boundaries. Further global and selective strain analysis is aided by spherical histogram visualization.

7.3. Expert Evaluation

Numerical models of the flow and strain field in subduction zones have two main purposes in geophysics research. First,
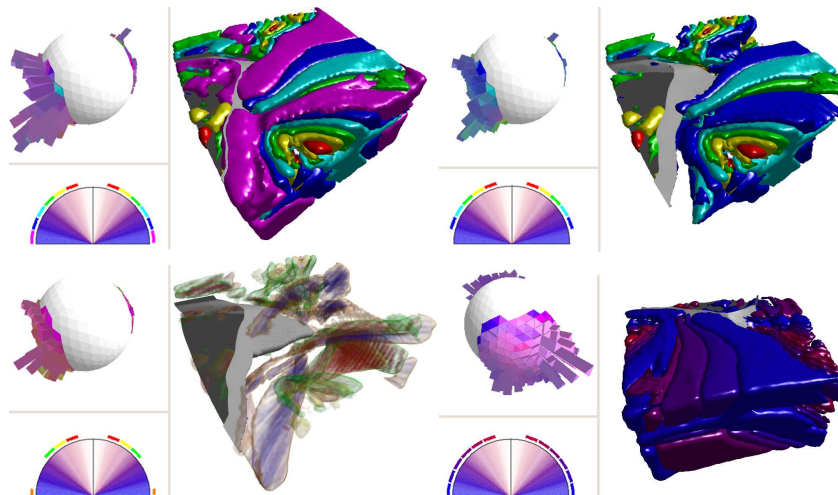
Figure 10: Segmentation f_a reveals large regions, where LPO and flow directions disagree. Selection and use of transparency support further analysis of volume properties. In contrast to f_o segmentation, histograms in alignment based segmentation often show no clear segmentation in orientation space. No region with full strain-velocity agreement is found, as indicated by radial graphs (full alignment represented by y-axis). Volume coloring according to average alignment (bottom right) allows easy identification of reliable and unreliable strain directions in the histogram.
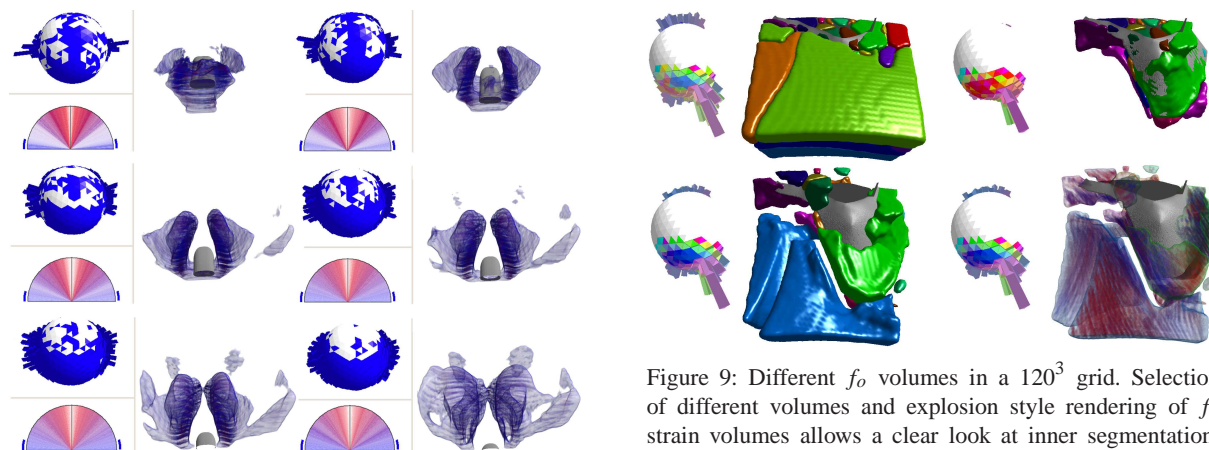

Figure 8: Left to right, top to bottom: Evolution of f_a region with maximal deviation between strain and flow. Strong orthogonal strain is observed along frontal lateral parts of the slab and weak orthogonal strain in lateral parts. Dominant dis-alignment direction is indicated by histograms and strain lines. Radial graphs show alignment of the selected region.

Figure 9: Different f_o volumes in a 120^3 grid. Selection of different volumes and explosion style rendering of f_o strain volumes allows a clear look at inner segmentation, where strain segmentation coincides with slab geometry. Additional transparent rendering reduces occlusion. Histogram display shows a dominant strain direction parallel to the slab.

using time-varying flow models we can examine how the 3D strain-field evolves as the geometry of a subducting plate and the induced flow change in time: this analysis gives us insight into how geophysical events change the strain field. Second, comparison of the flow and strain field from instantaneous flow models to observed seismic anisotropy for specific, real regions of the earth provides the only means of determining the actual geometry of flow in the mantle for the present day. The geometries and locations (relative to the sinking slab) of regions with uniform stretching directions

together with the information about the stretching direction and magnitude can be used to predict the fast axis orientations that would be observed at the surface, compare these with observations and link them to the mantle flow. This information bridges a gap between the seismologist and the geodynamicist allowing them to work iteratively to compare the results of numerical models and observations of fast axis in order to determine the pattern of flow in the mantle.

7.3.1. Time-Varying Flow

For the analysis of the time-varying flow models, visualizations of the segmentation of the strain-field and how this changes in time, provides an efficient means for character-

izing how the structure of the strain field changes with the evolving structure of the sinking plate. Here the visualizations provide clear indications of regions with similar strain-field characteristics, which are likely to form a strong LPO fabric along flow lines, as well as the boundaries between these regions where LPO will go through realignment, which can lead to weak LPO and observed seismic anisotropy. The 3D histograms visualized with the segmentation isosurfaces indicate the degree of misalignment of the strain field in adjacent regions, which is important for determining how weak the LPO will be in the transitional region.

In the example data set, the f_o segmentation clearly shows multiple regions with only moderately aligned strain-fields (separation in histogram in Figure 7) and their evolution over time. Orientation changes can be seen to be prevalent along paths of more complex (i.e., vortex lines) flow. This evolution occurs as the slab sinks deeper and steepens, changing its shape from concave down to concave up. This clear connection between the strain-field and changing geometry would have been difficult to recognize using standard techniques of plotting the maximum stretching orientations within the 3D volume for multiple time-steps and trying to recognize spatial patterns and changes in time.

7.3.2. Instantaneous Flow and Comparison to Observations

For the analysis of instantaneous flow models, our focus is on determining the flow pattern in the mantle through comparison of the strain field with indirect observation of the LPO (seismic anisotropy). In this case, it has been common to assume that the flow field is aligned with the strain-field, and therefore the fast-axis of seismic anisotropy indicates the flow directions. However, we know that this assumption breaks down in regions with complex 3D flow, like subduction zones. Therefore, visualization of the f_a segmentation, based on the relative alignment of the flow and strain field, provides a direct visual indication of where in the model flow and strain field are aligned, and a simple mapping from seismic anisotropy to flow is sufficient, and where the flow field may be strongly out of alignment, requiring more sophisticated analysis (volumes with red strain-lines in Figure 10). The tool also makes it easy to select display of volumes with different degrees of alignment, revealing the 3D structure of these volumes (see large misalignment volume in Figure 10). This is particularly important because a single observation of seismic anisotropy integrates the orientation of LPO along a seismic ray path that travels up through different depths of the mantle beneath the seismic station. Therefore, if there are strong changes in orientation of the strain field beneath a seismic station, the changes in orientation with depth have to be accounted for in analysis of the observations, which is lost in two-dimensional projections of the strain field.

In the example data set for the Alaska subduction zone, the strain field is the calculated infinite strain-axis (ISA) orientation [KR02, CBS07]. This same data set was previously analyzed and compared to surface observations of seismic anisotropy using 3D visualization of the ISA vector, with the flow vectors, as well as using maps of the directions at many depths [JB10]. Using the previous technique it was very difficult to identify regions with parallel alignment of the ISA and flow in 2D and 3D. It was particularly difficult to identify isolated regions of misalignment that changed rapidly with depth. The segmentation visualization developed here, makes such identification very efficient and through the histograms provides quantitative information on the degree of misalignment (strong change in alignment along outer parts of the data set as indicated by thin volumes in Figure 10). An interesting feature that can be identified by 3D strain analysis is a region of slab-parallel stretching surrounded by stretching that is caused by the poloidal flow (purple lateral volume in Figure 9). This region of slab-parallel stretching corresponds to the observations of seismic fast axis with similar alignment. This is an important example of stretching and lattice preferred orientation that is perpendicular to the dominate flow direction of the mantle [JB10]. Our results show that the presented extraction and visualization techniques are suitable for strain based analysis of time-varying and stationary flow. The examples analyzed in this work demonstrate that geophysical flow analysis benefits from these techniques by providing means of LPO discontinuity and flow alignment visualization, thus allowing detailed conclusions about the quality and confidence into flow reconstruction from LPO and formation of separate material sections.

8. Conclusion and Future Work

We have presented a method for automatic strain analysis in 3D flow data and its application to the field of geophysics. Our work contributes to the geophysics community by providing a more intuitive, 3D view of the data and supporting automatic analysis and segmentation of 3D strain. The methods developed in this work to extract and visualize regions with uniform stretching directions and the magnitude of stretching, provide an efficient and effective means of identifying regions with potentially strong LPO and improve the understanding of seismic measurements of LPO. The visualizations convey several key pieces of information: the geometry and locations of edges in the field of stretching directions, the magnitude and orientation of the stretching, and the relative behavior of mantle flow within each region. Thus, contributions of our work to visualization are the development of multi-volume visualization of interior and boundary representation for flow induced strain in instantaneous and time-varying flow fields, created by novel strain extraction and segmentation. While we have demonstrated the applicability and expressiveness of strain analysis in geophysics, we expect that many other application areas, such as industrial mixing, can benefit from a sophisticated strain field analysis in connection with existing vector field visualization techniques.

References

[BB10] BURKETT E. R., BILLEN M. I.: Three-dimensionality of slab detachment due to ridge-trench collision: Laterally simultaneous boudinage versus tear propagation. *Geochemistry, Geophysics and Geosystems 11* (2010), Q11012. 2, 9

[Bil08] BILLEN M. I.: Modeling the dynamics of subducting slabs. *Annu. Rev. Earth Planet. Sci. 36* (2008), 325–356. 1

[Bre65] BRESENHAM J. E.: Algorithm for computer control of a digital plotter. *IBM Systems Journal 4*, 1 (1965), 25–30. 4

[CBS07] CONRAD C. P., BEHN M. D., SILVER P. G.: Global mantle flow and the development of seismic anisotropy: Differences between the oceanic and continental upper mantle. *J. Geophys. Res. 112* (2007). 2, 3, 11

[CL93] CABRAL B., LEEDOM L. C.: Imaging vector fields using line integral convolution. In *SIGGRAPH '93: Proc. of the 20th annual Conference on Comput. Graph. and Interactive Techniques* (1993), pp. 263–270. 7

[EHK*04] ENGEL K., HADWIGER M., KNISS J. M., LEFOHN A. E., SALAMA C. R., WEISKOPF D.: Real-time volume graphics. In *SIGGRAPH '04: ACM SIGGRAPH 2004 Course Notes* (New York, NY, USA, 2004), ACM, p. 29. 2, 7

[Eve01] EVERITT C.: Interactive Order-Independent Transparency. NVidia, 2001. 6

[EYD02] ERLEBACHER G., YUEN D. A., DUBUFFET F.: Case study: visualization and analysis of high rayleigh number — 3d convection in the earth's mantle. In *VIS '02: Proc. of Vis. '02* (2002), pp. 493–496. 2

[GJL*09] GRUNDY E., JONES M. W., LARAMEE R. S., WILSON R. P., SHEPARD E. L. C.: Visualisation of Sensor Data from Animal Movement. *Comput. Graph. Forum 28*, 3 (2009), 815–822. 8

[Hal01] HALLER G.: Lagrangian structures and the rate of strain in a partition of two-dimensional turbulence. *Physics of Fluids 13*, 11 (2001), 3365–3385. 2

[HBH03] HADWIGER M., BERGER C., HAUSER H.: High-quality two-level volume rendering of segmented data sets on consumer graphics hardware. In *VIS '03: Proc. of Vis '03* (2003), pp. 301–308. 6

[HJYW03] HASHASH Y., JOHN I., YAO C., WOTRING D.: Glyph and hyperstreamline representation of stress and strain tensors and material constitutive response. *Internat. Journal for Numerical and Analytical Methods in Geomechanics 27*, 7 (2003), 603–626. 6

[HS05] HLAWITSCHKA M., SCHEUERMANN G.: Hot-lines: tracking lines in higher order tensor fields. In *VIS '05: Proc. of Vis '05* (2005), pp. 27–34. 8

[JB10] JADAMEC M., BILLEN M. I.: Reconciling Surface Plate Motions with Rapid 3D Mantle Flow around a Slab Edge. *Nature In Press* (2010). 2, 3, 4, 9, 11

[KJKS08] KARATO S., JUNG H., KATAYAMA I., SKEMER P.: Geodynamic significance of seismic anisotropy of the upper mantle: New insights from laboratory studies. *Annu. Rev. Earth Planet. Sci. 36* (2008), 59–95. 3

[KPH*09] KASTEN J., PETZ C., HOTZ I., NOACK B., HEGE H.-C.: Localized Finite-time Lyapunov Exponent for Unsteady Flow Analysis. In *Vision Modeling and Visualization* (2009), vol. 1, Universität Magdeburg, Inst. f. Simulation u. Graph., pp. 265–274. 2

[KR02] KAMINSKI É., RIBE N. M.: Timescales for the evolution of seismic anisotropy in mantle flow. *Geochem. Geophys. Geosyst. 3*, 1 (2002). 2, 5, 11

[LGALW09] LUIS-GARCÍA R., ALBEROLA-LÓPEZ C., WESTIN C.: Segmentation of Tensor Fields: Recent Advances and Perspectives. *Tensors in Image Processing and Computer Vision* (2009), 35–58. 5

[MvKK02] MCNAMARA A. K., VAN KEKEN P. E., KARATO S.-I.: Development of anisotropic structure in the Earth's lower mantle by solid-state convection. *Nature 416* (2002), 310–314. 2, 3

[NJP05] NEEMAN A., JEREMIC B., PANG A.: Visualizing tensor fields in geomechanics. In *Proc. of IEEE Vis 05* (oct. 2005), pp. 35–42. 2

[OHBKH09] OBERMAIER H., HERING-BERTRAM M., KUHNERT J., HAGEN H.: Volume Deformations in Grid-Less Flow Simulations. *Comput. Graph. Forum 28*, 3 (2009), 879–886. 2, 5

[RJF*09] RODRIGUES P., JALBA A., FILLARD P., VILANOVA A., TER HAAR ROMENY B.: A Multi-Resolution watershed-based approach for the segmentation of Diffusion Tensor Images. *MICCAI Workshop on Diffusion Modelling* (2009), 161–172. 2

[RM00] ROERDINK J., MEIJSTER A.: The Watershed Transform: Definitions, Algorithms and Parallelization Strategies. *Fundamenta Informaticae 41* (2000), 187–228. 6

[RS94] RUSSO R. M., SILVER P. G.: Trench-parallel flow beneath the Nazca Plate from seismic anisotropy. *Science 263*, 5150 (1994), 1105–1111. 3

[RTF*06] RÖSSLER F., TEJADA E., FANGMEIER T., ERTL T., KNAUFF M.: GPU-based Multi-Volume Rendering for the Visualization of Functional Brain Images. In *In Proc. of SimVis 2006* (2006), pp. 305–318. 6

[STS07] SCHULTZ T., THEISEL H., SEIDEL H.-P.: Segmentation of DT-MRI anisotropy isosurface. In *Proc. EuroVis 2007* (2007), pp. 187–194. 2

[Sub09] SUBRAMANIAN N. C.: *Convective Stretching And Applications To Mantle Mixing*. PhD Thesis. UC Davis, 2009. 2

[SWTH07] SAHNER J., WEINKAUF T., TEUBER N., HEGE H.-C.: Vortex and Strain Skeletons in Eulerian and Lagrangian Frames. *IEEE TVCG 13*, 5 (2007), 980–990. 2

[TGE97] TEITZEL C., GROSSO R., ERTL T.: Efficient and Reliable Integration Methods for Particle Tracing in Unsteady Flows on Discrete Meshes. In *Visualization in Scientific Computing '97* (1997), Springer, pp. 31–41. 4

[WEE02] WEISKOPF D., ENGEL K., ERTL T.: Volume clipping via per-fragment operations in texture-based volume visualization. In *VIS '02: Proc. of Vis. '02* (2002), pp. 93–100. 6

[WSMG06] WENK H.-R., SPEZIALE S., MCNAMARA A., GARNERO E. J.: Modeling lower mantle anisotropy development in a subducting slab. *Earth and Planetary Sci. Letters 245* (2006), 302–314. 2, 3

[ZiK95] ZHANG S., I. KARATO S.: Lattice preferred orientation of olivine aggregates deformed in simple shear. *Nature 375* (1995), 774–777. 2

[ZMB*03] ZHUKOV L., MUSETH K., BREEN D., WHITAKER R., BARR A. H.: Level Set Modeling and Segmentation of DT-MRI Brain Data. *J. Electron. Imaging 12* (2003), 125–133. 2

[ZTW06] ZIYAN U., TUCH D., WESTIN C.-F.: Segmentation of Thalamic Nuclei from DTI using Spectral Clustering. In *Ninth International Conference on Medical Image Computing and Computer-Assisted Intervention (MICCAI'06)* (Copenhagen, Denmark, October 2006), LNCS 4191, pp. 807–814. 5